Mass Spectrometry Imaging of Lipids using MALDI Coupled with Plasma-Based Post-Ionisation on a Trapped Ion Mobility Mass Spectrometer

Jesse A. Michael[1,2], Shadrack M. Mutuku[1,2], Boris Ucur[1], Tassiani Sarretto[1,2], Alan T. Maccarone[1], Marcel Niehaus[3], Adam J. Trevitt[1] and Shane R. Ellis[1,2]*

[1] Molecular Horizons and School of Chemistry and Molecular Bioscience, University of Wollongong, Northfields Ave, Wollongong, NSW 2522, Australia.

[2] Illawarra Health and Medical Research Institute, Northfields Ave, Wollongong, NSW 2522, Australia.

[3] Bruker Daltonics GmbH & Co. KG, Fahrenheitstr. 4, 28359, Bremen, Germany.

*to whom correspondence should be addressed

Email: sellis@uow.edu.au

Abstract

Here we report the development and optimization of a mass spectrometry imaging (MSI) platform that combines atmospheric-pressure matrix-assisted laser desorption/ionization platform with plasma post-ionization (AP-MALDI-PPI) and trapped ion mobility spectrometry (TIMS). We discuss optimal parameters for operating the source, characterize the behaviour of a variety of lipid classes in positive- and negative-ion modes and explore the capabilities for lipid imaging using murine brain tissue. The instrument generates high signal-to-noise for numerous lipid species, with mass spectra sharing many similarities to those obtained using laser post-ionization (MALDI-2). The system is especially well suited for detecting lipids such as phosphatidylethanolamine (PE) as well as numerous sphingolipid classes and glycerolipids. For the first time, the coupling of plasma-based post-ionization with ion mobility is presented and we show the value of ion mobility for the resolution and and identification of species within rich spectra that contain numerous isobaric/isomeric signals that are not resolved in the *m/z* dimension alone, including isomeric PE and demethylated phosphatidylcholine lipids produced by in-source fragmentation. The reported instrument provides a powerful and user-friendly approach for MSI of lipids.

Introduction

Matrix-assisted laser desorption/ionization-mass spectrometry imaging (MALDI-MSI) is a powerful label-free approach that allows imaging of many different molecular classes including metabolites/pharmaceuticals, lipids,[1, 2, 3] peptides/proteins[4, 5] and N-glycans[6] throughout biological samples such as thin tissue sections, plants,[7] and single cells.[8, 9] In recent years, the spatial resolution of commercial MALDI-MSI systems has improved dramatically to 5-10 µm, with bespoke systems capable of reaching ~1 µm spatial resolution.[8, 10, 11, 12] Lipids are one of the most widely interrogated biomolecules by MALDI-MSI, along with other common MSI methods such as secondary ion mass spectrometry (SIMS),[13, 14, 15] desorption electrospray ionization (DESI)[16, 17] and laser ablation electrospray ionization/matrix-assisted desorption electrospray ionisation.[18, 19] This is due to both the relative ease of ionization of several common lipid classes as well as the central role of lipid metabolism in countless biological processes and diseases.[20, 21]

MALDI analysis is conventionally performed under vacuum; however, atmospheric pressure (AP) arrangements are also used,[22, 23] having advantages including ease of sample exchange and a broader tolerance for analysis of volatile analytes and vacuum incompatible samples. In the context of lipid analysis, AP-MALDI approaches can also be advantageous for labile lipid species, such as gangliosides, that show reduced in-source fragmentation when ionized at AP.[24]

The analytical sensitivity of MALDI-MS is fundamentally limited by ionization efficiencies, i.e., the fraction of generated ions relative to desorbed neutrals. Ionization efficiencies are molecule- and source-dependent and have been reported to be in the range of 10^{-3}-10^{-9}.[25] Further limits to sensitivity include ion suppression effects whereby certain lipid species, such as PC in positive-ion mode analysis, can lower the ionization efficiencies of other lipid classes.[26] These phenomena limit both the achievable sensitivity and breadth of lipid

coverage obtained for MALDI-MSI experiments. Technologies that maximize ion yields from smaller sampling regions are a major focus of recent endeavours in the field, where there is a goal to improve the spatial resolution and encroach on the subcellular world while retaining the rich lipidomic and metabolomic data

To this goal, various post-ionization technologies have been developed in recent years that involve subjecting analytes to an additional ionization event subsequent to initial desorption/ionization. Arguably the most prominent, laser post-ionization (termed-MALDI-2) uses a second ultraviolet (UV) laser pulse with a wavelength below the two-photon ionization threshold of the matrix to irradiate the plume and induce a second MALDI-like event ~200-500 µm above the sample that is initiated by proton transfer from multiphoton-ionized matrix molecules/clusters.[27] MALDI-2 improves the sensitivities for many lipid classes by up to several orders of magnitude over conventional MALDI.[27, 28, 29] Vacuum-ultraviolet irradiation from radio-frequency-Krypton lamps has also recently been shown to promote soft post-ionization of lipids fostered by gas-phase charge transfer from single-photon ionized chemical dopants, producing similar spectral Information as MALDI-2.[30] Dielectric barrier discharge (DBD) is another promising technology to facilitate post-ionization in MSI. DBD devices can be coupled to the AP sampling capillary enabling efficient interaction of collected neutrals with ions formed in the cold plasma. These in-line devices, such as the commercially available soft ionization by chemical reaction in transfer (SICRIT) system, have been used for direct laser desorption (LD)-MSI of medicinal plants and zebrafish sections,[31] narcotics in fingernails,[32] small molecules in a pain killer tablet and a coffee bean,[33] and lipids in murine brain tissue.[34] Recently, matrix-free infrared laser ablation at atmospheric pressure combined with post-ionization by SICRIT was demonstrated for the MSI of metabolites and lipids in both fresh and formalin-fixed paraffin-embedded tissues.[35]

The addition of ion mobility technologies to MSI workflows is a promising approach that enables the resolution of isobaric and isomeric species and provides additional physical evidence that can be used for the assignment of features to known molecules. While the benefits of ion mobility for the MSI analysis of lipids are well established,[36] Soltwisch *et al* have recently documented the combination of trapped ion mobility spectrometry (TIMS) with post-ionization in the form of MALDI-2, finding a substantial increase in the number of detected features during MSI of rat brain and testis tissue.[37]

In this work we describe the development and optimization of a trapped ion mobility quadrupole time-of-flight mass spectrometer coupled with AP-MALDI and an in-line plasma-based post-ionization device (AP-MALDI-PPI). We demonstrate the capability of this system for detecting and imaging lipid species, investigate the type of ions generated for numerous lipid classes, and show the system offers high performance for the MSI of lipids at competitive spatial resolutions. For the first time, we show the coupling of a plasma-based post-ionization with an ion mobility-equipped mass spectrometer, and demonstrate that this combination is critical to resolving the rich spectra generated.

Methods

Details on materials, sample preparation and microscopy are provided in Supporting Information.

Instrument Design

All experiments were performed using a timsTOF Pro mass spectrometer (Bruker Daltonics, Bremen, Germany).[38] An overview of the instrument modification is shown in Figure 1. To enable AP-MALDI-MSI the instrument was equipped with the same MALDI stage, camera and Smartbeam 3D 355 nm laser as used on the timsTOF fleX instrument. These were mounted externally to the system on an optics breadboard, which allowed control of all MALDI functionality using timsControl and flexImaging. The laser was guided and focussed onto the sample using three dielectric-coated 355 nm mirrors and a 200 mm focal length lens (Figure 1). For MSI experiments, the laser output pulse energy was ca. 1.5 µJ as measured before the first mirror using a calibrated energy sensor (QE8SP-B-MTD0, Gentec-EO, Quebec, Canada). Under these conditions, the size of the ablation holes in the matrix were ca. 25 µm in diameter as measured by optical microscopy.

Desorbed ions and neutrals were collected using a heated inlet capillary (ID = 1 mm, ThermSys GmbH, Kahl am Main, Germany). The capillary was heated using two heating coils surrounding the front and rear halves of the capillary length, and these coils were powered by two adjustable DC power supplies. The temperature was monitored by a thermocouple installed near the middle of the capillary. The SICRIT® device (Plasmion GmbH, Augsburg, Germany) was installed according to the manufacturer's instructions between the heated inlet capillary and the resistive glass capillary that forms part of the standard ESI source. The distance between the sample and the mouth of the inlet capillary was ~2 mm.
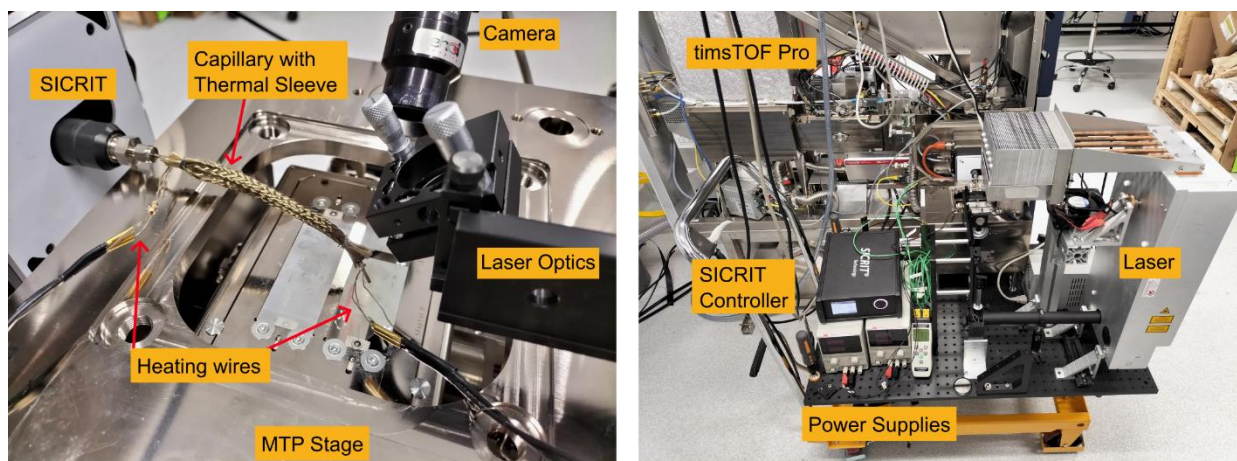
Figure 1. *Ion source design for timsTOF Pro coupled with AP-MALDI and SICRIT plasma-post-ionization device. Left: Close-up of ion source showing the with SICRIT device attached to heated capillary, camera, laser optics and Bruker MTP stage. Right: View of SICRIT controller, dual power sources for capillary, laser optics and Smartbeam 3D laser on height-adjustable platform, in front of timsTOF instrument.*

Data Acquisition: The instrument was controlled using timsControl (Client version 3.0.0) and flexImaging (Version 7.0, Bruker Daltonics GmbH & Co. KG). A summary of key instrument settings used to acquire the presented data is provided in Supporting Information Table S1. Mass calibration was performed using either known endogenous lipid signals or background polydimethylsiloxane (PDMS) signals. Ion mobility calibration was performed by MALDI of Agilent ESI-L low-concentration tuning mix, prepared as a 2.5x dilution with 5 mg/ml of DHA in methanol and sprayed onto glass slides using a TM sprayer (HTX Technologies LLC, Chapel Hill, North Carolina; 1200 mm/min velocity, 16 passes, 30°C, 5s drying time, 60 µL/min).

For optimizing the operating parameters for MSI experiments, acquisitions of approximately 300 pixels were recorded from interweaved regions on the same section of liver homogenate with a single parameter varied per acquisition. Interweaving was performed by using the same region drawn in flexImaging with 160 µm pixel size displaced by successive 40 µm increments in X and Y directions.

Lipid standard data was acquired as a single region per polarity covering one of each spots on a Bruker MTP 384 target plate with 60 µm raster size.

Brain tissue imaging experiments were performed at spatial resolutions of 20 or 30 µm. TIMS-MSI data was acquired across a $1/K_0$ range of 1.15-1.60 using 1000 ms ramp time. Further acquisition parameters are provided in Supporting Information Table S1.

MS/MS data of selected peaks were acquired by manually recording single pixels at four different collision energy values and 1 Da isolation width, and exporting the summed spectra from timsControl.

Data Analysis: All data sets had a lock-mass recalibration applied in DataAnalysis (Version 5.3, Bruker Daltonik GmbH) and were loaded into SCiLS Lab (Version 2022b Pro, Bruker Daltonics GmbH & Co. KG) with 'Reflector TOF' *m/z* binning settings of 3 mDa at *m/z* 1000.

For liver homogenate, a sliding intensity cutoff was used to pick approximately 2,500 features (*m/z* values) from each combined set, and an additional list of theoretical mass values for lipid ions was imported as a target list. Lipid class signal intensities were taken as the mean of five target lipid masses per class (Supporting Information Table S2) and a combined ion metric was produced by summing intensities from all peaks between *m/z* 700-1000. Intensity values (6 ppm tolerance) were exported from SCiLS in .csv format and imported into Matlab 2019b (The MathWorks, Inc.) for plotting.

Regions of Interest for each individual lipid standard spot were manually drawn in SCiLS and averaged spectra exported and used for analysis.

For mouse brain acquisitions, ion images were produced in SCiLS Lab using 6 or 8 ppm tolerance, total ion current normalization and 99% quantile hot-spot removal, unless

otherwise specified. Mobility-*m/z* heatmaps were exported as a full-dataset average from DataAnalysis.

Lipid Nomenclature: We endeavour to adopt recommendations for lipid annotations and fragment descriptions based on current guidelines,[39, 40] albeit by using the common convention of enclosing carbon chain information in brackets (e.g. [PE(40:6)+H]$^+$) for reading clarity when specifying fragments/adducts. We will use "Diox" in a manner similar to lipid classes for the series of dioxolane fragments which would otherwise be labelled as phospholipid headgroup losses or DG-related molecules (e.g. [Diox(40:6)+H]+ is equivalent to [PC(40:6)-PC(183)+H]$^+$ and [DG(40:6)-H$_2$O+H]$^+$).

Results & Discussion

Influence of Key Source Parameters

We first explored the influence of several key parameters on lipid signals generated from AP-MALDI-PPI of rat liver tissue homogenate, with the results shown in Figure 2. As readouts of lipid signal intensities, we monitored a metric representing total ion signal between m/z 700-1000, where the majority of lipid signal is expected, as well as several key detectable lipid classes, namely protonated phosphatidylethanolamines (PE); triacylglycerols (TG); ceramides (Cer), phosphatidic acids (PA), phosphatidylcholines (PC) and dioxolanes (Diox, a prominent class of fragment - see below). Each class was calculated as the average of five selected species, provided in Supporting Information Table S2. The influence of the SICRIT RF amplitude is shown in Figure 2a and reveals an optimal value of 1500-1600 V_{p-p} that is in line with previous studies.[33, 34, 35] Between 10-20 kHz, the RF frequency had little effect on the overall signal (Figure 2b). Surprisingly, with the SICRIT device turned off, virtually no ion signal was observed even for elevated laser powers beyond those typically used for MALDI, where generation of MALDI-like ions would be expected (Supporting Information Figure S1). We hypothesize this is due to the neutralization of MALDI-generated ions within the heated steel capillary, while neutrals are passed through to become subsequently ionized in the plasma region. This is in contrast to recent plasma-based post-ionization studies using the same SCIRIT device that reported low intensity lipid signals in the absence of a plasma that resembled the common ions observed from tissue using MALDI (i.e., alkali adducts of PC lipids).[34]

A heated inlet capillary is an essential requirement for generating abundant lipid signals. As highlighted in Figure 2c no lipid signal is observed until the inlet has reached 200 ˚C with a maximum signal between m/z 700-1000 observed at ~350 ˚C before beginning to decrease. Interestingly, there is a lipid-class dependence on the optimal operating temperature;

protonated PE lipids give the highest signals at ~375 ˚C, whereas protonated TGs are highest at ~275 ˚C. Such class-specific temperature dependence has also been reported using IR desorption and SICRIT.[35]
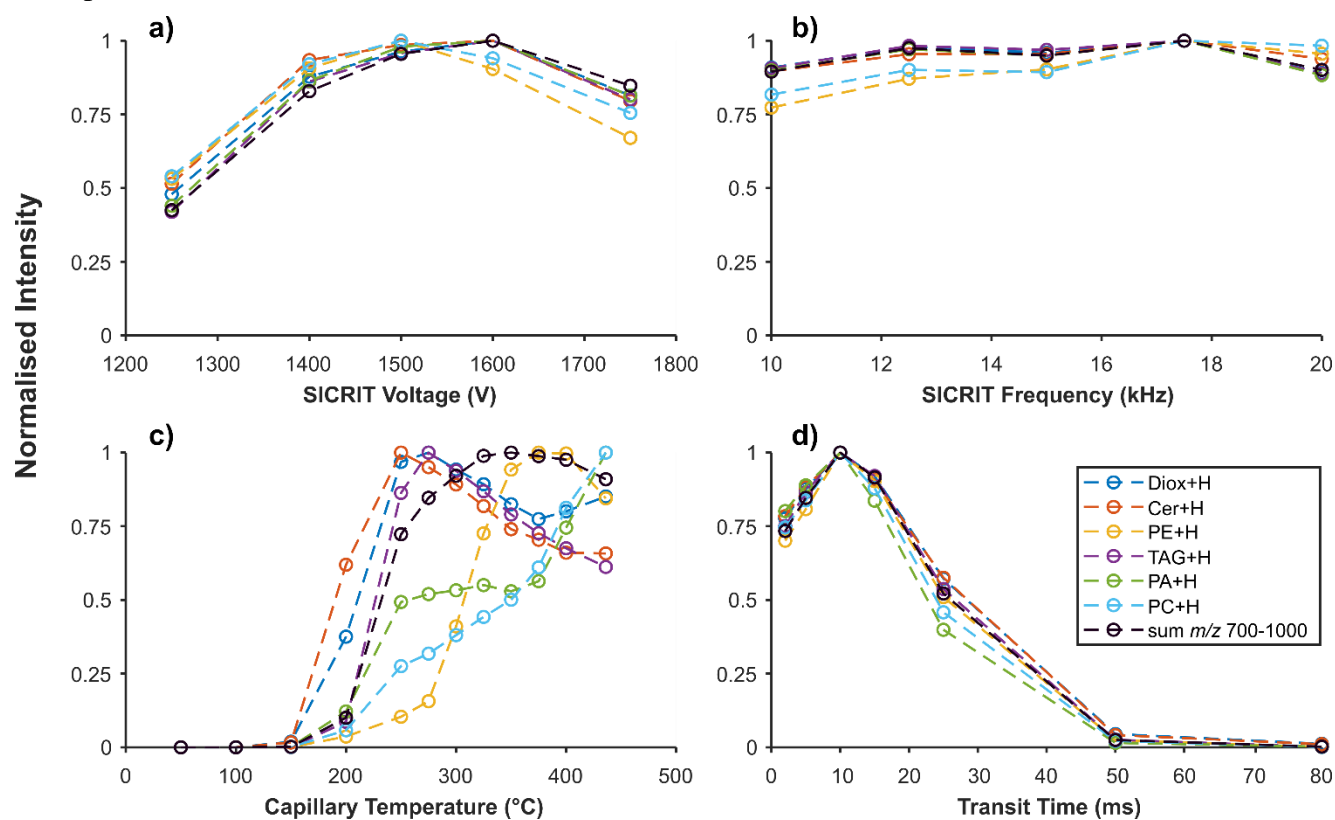

Figure 2. *Relationship of lipid signal intensities with various ion source parameters. (a) SICRIT RF amplitude, (b) SICRIT RF frequency, (c) Temperature at centre of inlet capillary, and (d) ion transit time setting. Lipid class signals are the sum of five representative species described in Supporting Information Table S2.*

Finally, the influence of the ion transit time was investigated (Figure 2d). The transit time is a critical parameter that defines the time delay between the laser pulse and the recording of ion detector output by the digitizer. Poorly optimized settings can result in large fractions of the generated ion packet not being recorded. In the standard timsTOF fleX instrument where MALDI is performed under vacuum at a pressure of ~3 mBar, the transit time is ~3 ms, which accounts for the time the analyte to travel from the sample through all ion optics before reaching the detector. In the setup described here, laser desorption is performed at AP and ions must

travel through the heated inlet capillary, the SICRIT device, and the standard resistance glass capillary before being deflected into the first ion funnel. Thus longer transit times are expected, and we find an optimal value of 10 ms (Figure 2d).

In positive-ion mode, a series of ions having an m/z that resembles $[DG+H-H_2O]^+$ were observed. These are a familiar headgroup-loss fragmentation product from phospholipids (or acyl loss from TGs) that contain a dioxolane moiety on the backbone[41, 42] and are referred to here as dioxolanes. Being fragmentation products, they are nominally undesirable but were present at substantial levels under all tested parameters. As these are detected in greater abundance than typically observed under ESI or MALDI we suspect they are formed by events in the plasma region of the source. A finite voltage gradient through the collision cell is required for the ions to traverse through collision cell. We observe that intensity of desired lipid ions peaks at a collision energy of 8 eV, while dioxolanes continue to increase steadily (Supporting Information Figure S2), and this result is compatible with the understanding that fragmentation is occurring in the source but with subsequent activation within the instrument approaching values typical under MS/MS. In negative-ion mode, increasing collision energy results in decreasing intensity of nitric acid adducts (see below) and an increase in deprotonated ions (data not shown).

In accord with previous reports on ambient post-ionization techniques,[34, 43] the major background peaks in positive-ion mode (Supporting Information Figure S1) match documented values for PDMS.[44] This substance is ubiquitous within laboratory air,[45] and the signal is proportional to ion accumulation time. While previous AP-PPI studies have considered ambient air contaminants troublesome, and worked to limit them through the use of transfer capillaries[34] or enclosed ablation cells with pure gases,[33] we find that these ions have very low intensity during MSI of tissue and their presence may even provide value as lock-mass calibration ions (Supporting Information Figure S2).

Evaluation of lipid coverage using standards

Next, we investigated the capabilities of the laser desorption/plasma post-ionization setup to detect specific lipid classes using a series of synthetic standards spotted onto a target plate with DHA, including an EquiSPLASH mixture containing deuterated lipids from 13 lipid classes at the same mass concentration (see Methods and Supporting Information Table S3). In positive-ion mode (Figure 3a), protonated species were again predominant with little signal arising from sodiated or potassiated adducts. This is consistent with previous publications featuring PPI[34], and the understanding that ionization occurs via charge transfer from species within the plasma, such as protonated water clusters.[46] Surprisingly, PC, often the main lipid species detected in positive-ion mode MALDI-MSI, was detected with very low signal intensity ([M+H]$^+$, *m/z* 753.615). However, a corresponding fragment was observed at *m/z* 739.598, representing a net loss of CH_2 from the protonated species. While investigation of the mechanism of fragmentation is beyond the scope of this work, demethylation via non-covalent anion adduction is a known fragmentation pathway for PCs[47] and has also been reported for MALDI-2.[28] We speculate that the PC is demethylated at the cationic quaternary nitrogen and protonated twice to yield a net positive charged dimethyl-PE, annotated here as [M-CH$_3$+2H]$^+$ (although the exact order of events is unknown, see Supporting Information Scheme 1). Sphingomyelin (SM), which also has a phosphocholine moiety, was also predominantly observed as the [M-CH$_3$+2H]$^+$ ion at *m/z* 724.631. PE was readily detected as the expected [M+H]$^+$ ion at *m/z* 711.577. The TG, diacylglycerol (DG) and cholesterol ester (CE) species were detected as both protonated and ammoniated forms, while monoacylglycerol (MG) was detected as the protonated ion. The observation of protonated versions of these molecules is unusual given their low proton affinities, and they are possibly formed by the sequential loss of NH_3 from the [M+NH$_4$]$^+$ ions. CE also appears to undergo in-source fragmentation to produce the cholesterol-related [Chol+H-H$_2$O]$^+$ ion at *m/z* 369.351, as has also been observed

under MALDI-2.[29] Two of the highest lipid-related peaks correspond to Cer in the form of [M+H]$^+$ and [M+H-H$_2$O]$^+$, suggesting this species is well-ionized by this approach. Also of note was the abundant signal at *m/z* 570.548 corresponding to the 15:0-18:1[7D] dioxolane that can be formed upon headgroup loss from any of the glycerophospholipid or TG standards (Supporting Information Scheme 2).
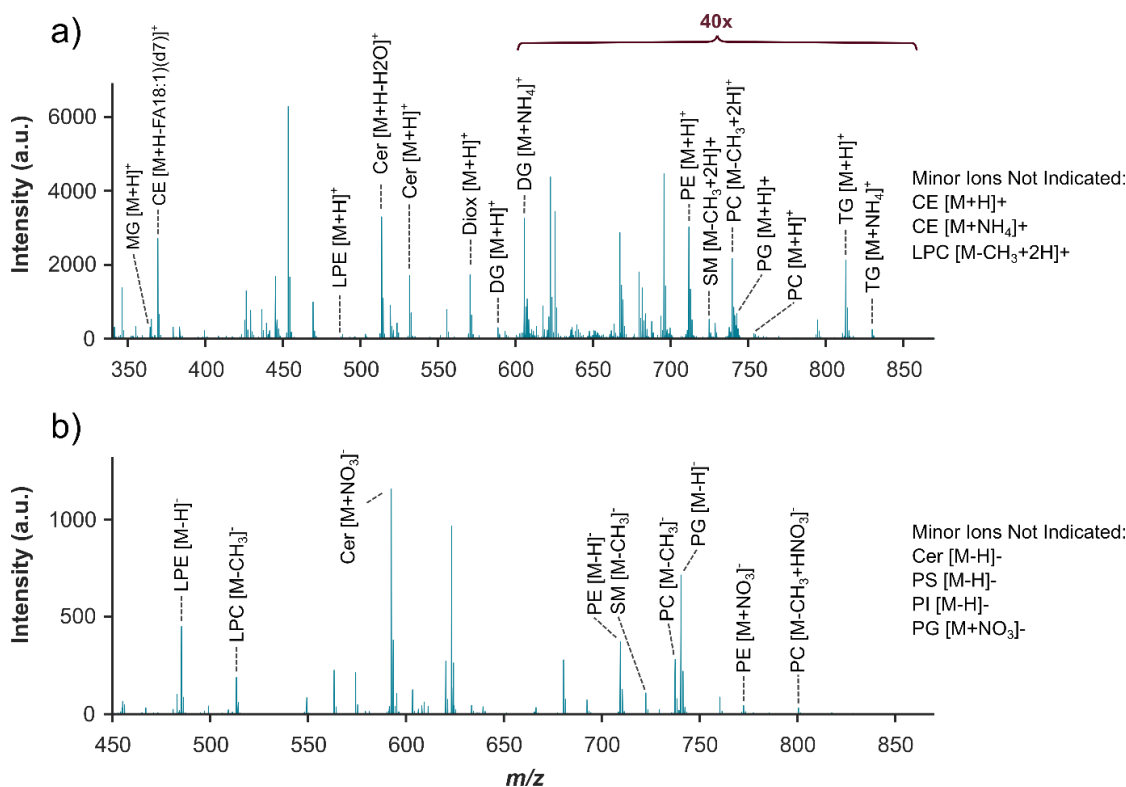

Figure 3. Average spectra obtained from analysis of EquiSPLASH lipid mixture in positive (a) and negative (b) ion modes. Annotations are based on accurate mass within 5ppm. Composition of the EquiSPLASH is provided in Supporting Information Table S3.

The corresponding negative-ion mode data from the EquiSPLASH mixture is shown in Figure 3b. In addition to the expected [M-H]$^-$ ions observed for many species (albeit some at low intensity), some lipids were also detected as nitrate adducts ([M+NO$_3$]$^-$). For example, the abundant peak at *m/z* 592.340 corresponds to the nitrate adduct of the ceramide species, observed at 3 orders of magnitude higher intensity than the deprotonated ion. MS/MS of these adducts (data not shown) results in a neutral loss of 62.996 Da (nitric acid, HNO$_3$) and could

arise due to the availability of HNO_3/NO_3^- species known to be present due to dielectric barrier discharge of gas environments containing nitrogen and oxygen.[48] Demethylation of PC and SM was also observed in negative-ion mode to produce $[M-CH_3]^-$ ions. Phosphatidylglycerol (PG) appears with moderate abundance in deprotonated form, while minor peaks are observed for deprotonated phosphatidylinositol (PI) and phosphatidylserine (PS).

To further understand the detection and in-source fragmentation pathways of different lipid classes, we also analyzed a series of individual lipid standards, the results of which are provided in Supporting Information Figures S3 & S4. Here we will focus on several key observations. First, in the positive-ion mode, all standards exhibited some in-source fragmentation to an extent and nature that varied dramatically between different classes. For all glycerophospholipid classes, dioxolane species were observed as a major fragmentation product. Intact $[M+H]^+$ ions were observed only at low intensity for PG and PI standards, and unobserved for PS. Consistent with data shown in Figure 3a, PE exhibited the least fragmentation, with the intact protonated species dominating the signal. Galactosylceramide (GalCer) produced an intense signal for the protonated ion, and low intensity fragments corresponding to $[M+H-H_2O]^+$ the neutral loss of galactose. Analysis of the PC standard yielded the most intense signal for the dioxolane fragment suggesting that PC is the major contributor to this class of ion in the mixed-lipid conditions of our other analyses herein. A minor peak for $[M+H]^+$ was observed, along with fragments corresponding to $[M-CH_3+2H]^+$ and $[M-(CH_3)_3+4H]^+$.

Generally consistent with data in Figure 3, negative mode analysis of PE, PG, PI and PS yielded $[M-H]^-$ ions with varying intensities, while the PE was also observed as $[M+NO_3]^-$ and the GalCer was essentially exclusively observed as the abundant nitrate adduct (Supporting Information Figure S4). The PC spectra is dominated by several fragmentation products that appear to relate to progressive losses from the headgroup. Together, the above data demonstrate

that while lipid analysis using the in-line plasma source for post-ionization is complex and can produce extensive in-source fragments for some lipid species, phospholipids such as PE, TG, DG and sphingolipids such as Cer and HexCer appear well suited for this technique.

Mass Spectrometry Imaging

We next explored the application of the AP-MALDI-PPI-equipped timsTOF for lipid imaging. Figure 4 shows positive-ion mode MSI data obtained from mouse brain tissue at a pixel size of 20 µm. At the laser spot sizes achieved, this corresponds to slight oversampling. Representative single-pixel spectra are provided in Figure S5 in the Supporting Information. The averaged mass spectrum is shown in Figure 4a and reveals the detection of numerous lipid species with excellent signal-to-noise, and sharing similarities with data obtained using MALDI-2 and other post-ionization methods where protonated PE and HexCer lipids produce the most intense signals[27, 30, 34]. When analyzed using the METASPACE annotation engine[49] against the LIPID MAPS database, 351 *m/z* values with distributions specific to on-tissue regions could be assigned to potential lipid species with a 10% false-discovery rate and < 10% off tissue probability (295 peak are annotated at < 1% off tissue probability). This demonstrates

the high sensitivity of the method toward many lipid classes and, consistent with earlier work

and that plasma post-ionization using SICRIT is a competitive ionization method for MSI.
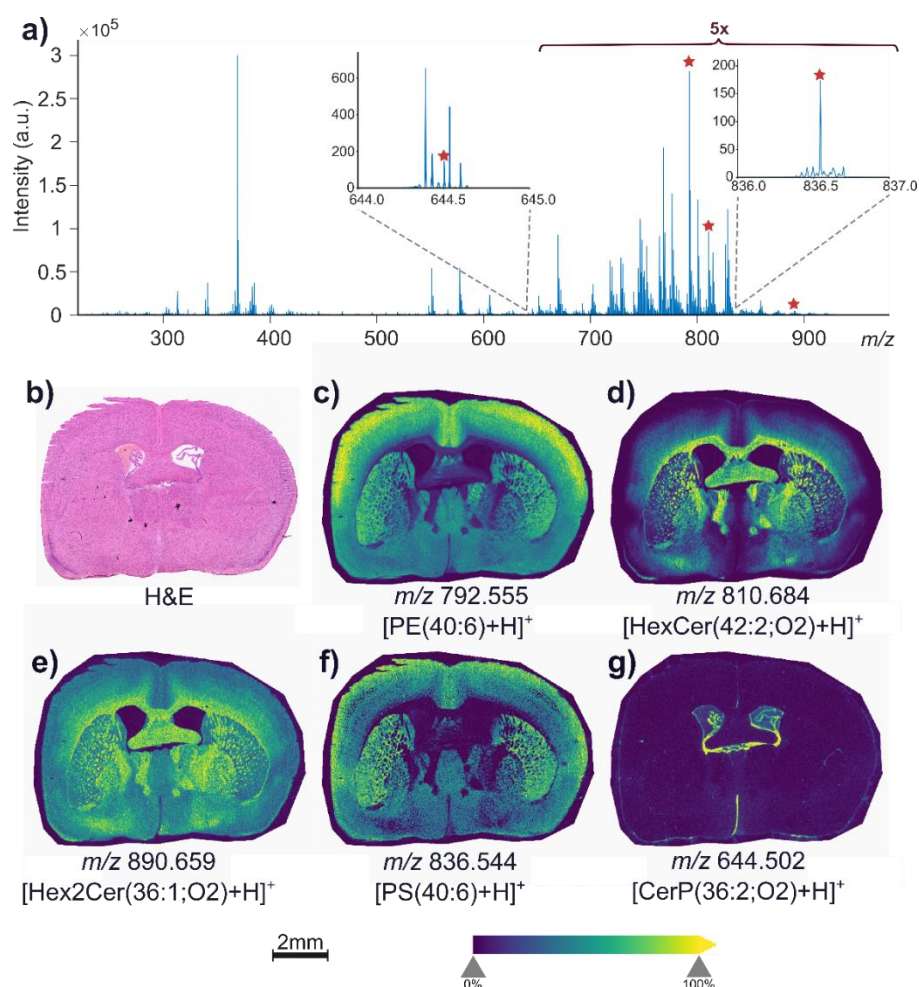

Figure 4. Positive-ion mode mass spectrometry imaging of mouse brain tissue at 20 µm pixel size. (a) Average mass spectrum measured from mouse brain tissue. Note the 5-fold magnification above *m/z* 650. Insets show two enlarged *m/z* regions demonstrating the dynamic range (no intensity magnification applied to insets). (b) Optical image of post-MSI tissue stained with H&E. (c-g) ion images of five selected ions indicated by red stars in (a) and corresponding to [M+H]+ ions of (c) PE(40:6), (d) HexCer(42:2;O2), (e) Hex2Cer(36:1;O2), (f) PS(40:6) and (g) CerP(36:2;O2). All ions are detected within 5 ppm of their theoretical *m/z* value and all ion images generated using +/-8 ppm mass tolerance, total-ion current normalization and hotspot removal (99% quantile).

The post-MSI H&E stained tissue section is shown in Figure 4b, whilst the distribution

of five selected lipid species (marked with red stars in Figure 4a) are shown in Figure 4c-g.

The ion at *m/z* 792.553 is assigned to $[PE(40:6)+H]^+$ and is distributed predominately

throughout the grey matter with the highest signal in the cortex, while The HexCer species

[HexCer(42:2;O2)+H]$^+$ (Figure 4d) is localized within the myelin-rich white matter. The low abundance Hex2Cer species (Figure 4e, likely lactosylceramide) is detected throughout most of the brain section but with the highest intensity within the white matter. Interestingly PS(40:6) was detected as the protonated ion and localized primarily within the grey matter (Figure 4f), even though no protonated signal was detected when analyzing a PS standard (see above). The identity of this ion was confirmed with MS/MS (Supporting Information Figure S6). Protonated PS lipids were also detected from brain tissue in earlier work using plasma post-ionization.[34] This could indicate the ionization of lipids desorbed from complex samples like tissue sections is different and possibly favourable compared to analyzing simple standard mixtures. We note that despite [PS(40:6)+H]$^+$ being only 0.3% of the intensity of [PE(40:6)+H]$^+$ within the averaged spectra, and only <0.001% of the intensity of the base peak at m/z 369.352 assigned to [Chol+H-H$_2$O]$^+$, it still yields a high contrast ion image, thereby demonstrating the high dynamic range of this technique. Figure 4g shows the localization of another sphingolipid, the ceramide-1-phosphate CerP(36:2;O2), to the veins in the lateral ventricles of the brain, again highlighting the suitability of this approach for imaging sphingolipids.

MSI data was also acquired in negative mode with a 30 µm pixel size. Similar to positive mode and the data from lipid standards, we find that the spectra is rich in peaks assigned as PEs and sphingolipids in the form of deprotonated ions and nitrate adducts (data not shown, METASPACE links provided in Data Availability section).

We also observed signal carryover for some analyte ions[35]. This effect is likely caused by the accumulation and release of some analytes within the heated inlet capillary and is most significant for a number of lower m/z ions like cholesterol and vitamin D, and to a lesser extent, the dioxolane fragments. The timescales of these processes were investigated by manually blocking the MALDI laser during a line scan and monitoring the intensity of several ions. The

results are provided in Supporting Information Figure S7 and reveal that the $[Chol+H-H_2O]^+$ signal intensity decays by ~75% by the subsequent pixel (approximately 100 ms) and then persists for many seconds at reduced levels. This process causes a linear blur in the generated ion images. In contrast, dioxolane fragments decay to 1-2% of the signal intensity by the subsequent pixel and then persist at this very low level, displaying a much milder level of blur. Importantly, signals for most features, including all phospholipids, TGs and sphingolipids have no detectable carryover between adjacent pixels.

Addition of Ion Mobility to MSI with plasma-based post-ionization

The experimental setup has allowed us to utilize trapped ion mobility for plasma-based post-ionization, and we obtained a TIMS-enabled dataset on mouse brain with representative single spectra shown in Supporting Information Figure S8. Given the rich lipidomic spectra generated from tissue (e.g., Figure 3), ion mobility is expected to aid in the resolution of inevitable isobaric and isomeric species. Here we will present two advantages of ion mobility applied to MSI using plasma-based post-ionization, namely (i) the resolution of isomeric $[PE+H]^+$ and $[PC-CH_3+2H]^+$ ions; and (ii) enabling the extraction of ion images for additional molecular features among complex isobaric mixtures that would otherwise remain unresolved in the absence of ion mobility.
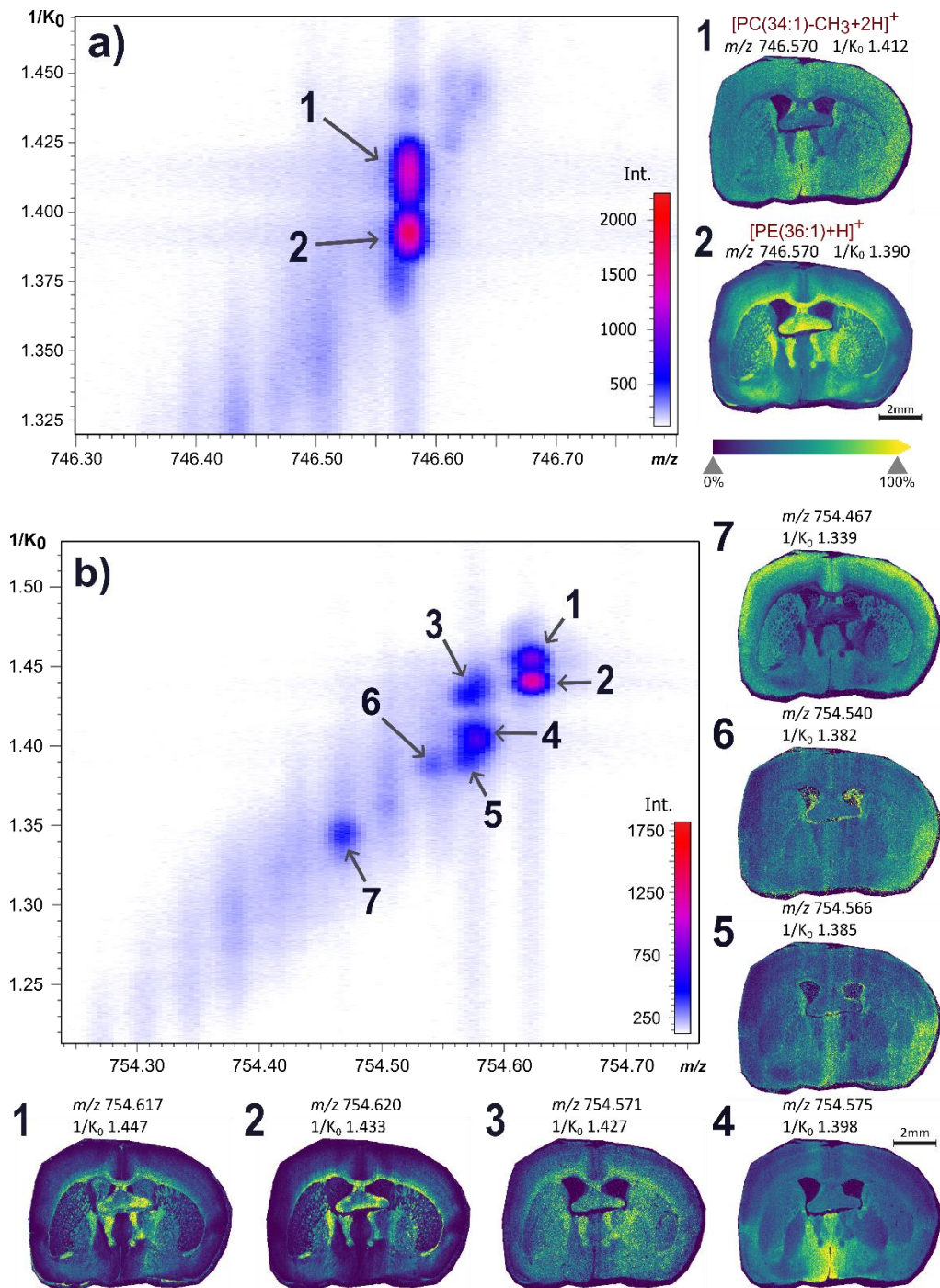
Figure 5: Trapped-ion mobility (TIMS) allows resolution of isomeric and isobaric ions generated by plasma post-ionization during MSI acquisition on mouse brain. (a) TIMS resolution of isomeric [PE(36:1)+H]$^+$ and the PC fragment [PC(34:1)-CH$_3$+2H]$^+$. Mobility resolved ion images are shown on the right. (b) TIMS resolution of eight ion features detected between m/z 754.45-754.7. Mobility resolved ion images are shown below and on the right. All ion images are generated using a +/-6 ppm mass tolerance, +/-0.006 1/K$_0$, total-ion current normalization and hotspot removal (99% quantile). Scale bar 2mm.

One of the surprising observations from the lipid standards outlined above was the low intensity observed for intact PC lipids and the detection of the fragment $[PC-CH_3+2H]^+$. These fragments resemble the native lipid class known as dimethyl-PE (DMPE, or PE-NMe2) that exist as intermediates in the enzymatic conversion between PC and PE, and are isomeric with PE lipids containing an additional two methylene groups on the acyl chains (e.g., $[PC(34:1)-CH_3+2H]^+$ is isomeric with $[PE(36:1)+H]^+$). Given the high abundance of PE and PC lipids in most tissues, these isomeric overlaps are expected throughout an MSI dataset. Figure 5a shows the ion mobility heat map with two isomeric features present at *m/z* 746.570. The TIMS-MS/MS data from this ion is provided in Supporting Information Figure S9. A fragment ion at *m/z* 577.519 is observed with a $1/K_0$ of 1.415 and is assigned to the neutral loss of a DMPE headgroup, while another fragment ion at *m/z* 605.550 is observed at the lower $1/K_0$ value of 1.395 and attributable to the neutral loss of the PE headgroup. These data thus allow assignment of the high $1/K_0$ feature in Figure 5a as $[PC(34:1)-CH_3+2H]^+$ and the low $1/K_0$ feature as $[PE(36:1)+H]^+$. The corresponding mobility-resolved ion images are shown on the left in Figure 5a, with each revealing distinct distributions throughout the mouse brain section. Analogous separation of $[PC-CH_3+2H]^+$ and $[PE+H]^+$ isomers was observed for numerous other isomeric pairs and additional examples are provided in Supporting Information Figure S10. In each case, TIMS-MS/MS reveal the low $1/K_0$ feature to correspond to the PE species. A further demonstration of the ability of TIMS to resolve more complex spectra is given in Figure 5b, where 7 distinct isobaric features are observed between *m/z* 754.45-754.70, including features not resolved in the *m/z* dimension (e.g., features 1 and 2, and 3, 4 and 5).

Conclusion

In this study we have presented a new instrumental concept for MSI that incorporates a timsTOF mass spectrometer equipped with an AP-MALDI ion source and plasma post-ionization. In this approach, the matrix acts only to promote the laser desorption of species from the sample surface, which are then collected by a heated inlet capillary and ionized by reactive species generated by the cold plasma. Despite technological differences, spectra generated from mouse brain tissue share similarities with MALDI-2 and other post-ionization approaches in that rich lipid spectra are generated with PE and HexCer lipid classes being well-represented and protonated ions predominating over alkali adducts. This suggests some commonalities in the ionization mechanisms of various post-ionization methods in the form of charge transfer to analyte from abundant background reactants.[27, 30] An advantage of plasma post-ionisation using SICRIT compared to MALDI-2 is the reduced dependency of alignment issues (e.g., MALDI-2 laser alignment) that makes it easier to acquire optimal data quality and post-ionisation efficiency.

Analysis of lipid standards revealed several surprising observations, including strong fragmentation of some lipid species such as PC, and abundant nitrate adducts in negative-ion mode. Overall, the current design appears well-suited for analyzing PE, neutral sphingolipids and TGs, but also generates signals for many other species. The addition of trapped-ion mobility facilitated the resolution of ions not resolved using *m/z* alone and aided in the resolution of the rich spectra that are generated. Of note, TIMS allowed the separation of $[PC-CH_3+2H]^+$ ions that are isomeric with PE lipids, thus enabling this mobility-resolved fragment to be used as a readout for PC lipids. The main limitation of sensitivity is likely the collection and transfer of neutral molecules through the heated capillary, in addition to reduced intact ion signals for some species due to fragmentation. Further improvements are likely to be found by

optimizing ion and neutral transfer conditions through the inlet capillary and control over in-source fragmentation processes.

In summary, our results demonstrate plasma-post-ionization coupled with UV laser desorption and TIMS is a promising and user-friendly approach for imaging lipids and metabolites, including those not well ionized by traditional MSI methods.

Data availability

MSI datasets are available on Metaspace (https://metaspace2020.eu/project/michael-2022). Raw data is available from the authors upon request.

References

(1) Zemski Berry, K. A.; Hankin, J. A.; Barkley, R. M.; Spraggins, J. M.; Caprioli, R. M.; Murphy, R. C. MALDI Imaging of Lipid Biochemistry in Tissues by Mass Spectrometry. *Chem. Rev.* **2011**, *111* (10), 6491-6512.

(2) Bowman, A. P.; Heeren, R. M. A.; Ellis, S. R. Advances in mass spectrometry imaging enabling observation of localised lipid biochemistry within tissues. *TrAC, Trends Anal. Chem.* **2019**, *120*.

(3) Buchberger, A. R.; DeLaney, K.; Johnson, J.; Li, L. Mass Spectrometry Imaging: A Review of Emerging Advancements and Future Insights. *Anal. Chem.* **2018**, *90* (1), 240-265.

(4) Angel, P. M.; Baldwin, H. S.; Gottlieb Sen, D.; Su, Y. R.; Mayer, J. E.; Bichell, D.; Drake, R. R. Advances in MALDI imaging mass spectrometry of proteins in cardiac tissue, including the heart valve. *Biochim. Biophys. Acta* **2017**, *1865* (7), 927-935.

(5) Piga, I.; Heijs, B.; Nicolardi, S.; Giusti, L.; Marselli, L.; Marchetti, P., . . . McDonnell, L. A. Ultra-high resolution MALDI-FTICR-MSI analysis of intact proteins in mouse and human pancreas tissue. *Int. J. Mass spectrom.* **2019**, *437*, 10-16.

(6) Drake, R. R.; Powers, T. W.; Jones, E. E.; Bruner, E.; Mehta, A. S.; Angel, P. M. Chapter Four - MALDI Mass Spectrometry Imaging of N-Linked Glycans in Cancer Tissues. In *Advances in Cancer Research*, Drake, R. R., McDonnell, L. A. Eds.; Vol. 134; Academic Press, 2017; pp 85-116.

(7) Ajith, A.; Milnes, P. J.; Johnson, G. N.; Lockyer, N. P. Mass Spectrometry Imaging for Spatial Chemical Profiling of Vegetative Parts of Plants. *Plants* **2022**, *11* (9), 1234.

(8) Bien, T.; Bessler, S.; Dreisewerd, K.; Soltwisch, J. Transmission-Mode MALDI Mass Spectrometry Imaging of Single Cells: Optimizing Sample Preparation Protocols. *Anal. Chem.* **2021**, *93* (10), 4513-4520.

(9) Zhu, X.; Xu, T.; Peng, C.; Wu, S. Advances in MALDI Mass Spectrometry Imaging Single Cell and Tissues. *Front. Chem.* **2022**, *9*, Review.

(10) Kompauer, M.; Heiles, S.; Spengler, B. Atmospheric pressure MALDI mass spectrometry imaging of tissues and cells at 1.4-μm lateral resolution. *Nat. Methods* **2017**, *14* (1), 90-96.

(11) Zavalin, A.; Yang, J.; Hayden, K.; Vestal, M.; Caprioli, R. M. Tissue protein imaging at 1 μm laser spot diameter for high spatial resolution and high imaging speed using transmission geometry MALDI TOF MS. *Anal. Bioanal. Chem.* **2015**, *407* (8), 2337-2342.

(12) Niehaus, M.; Soltwisch, J.; Belov, M. E.; Dreisewerd, K. Transmission-mode MALDI-2 mass spectrometry imaging of cells and tissues at subcellular resolution. *Nat. Methods* **2019**, *16* (9), 925-931.

(13) Passarelli, M. K.; Winograd, N. Lipid imaging with time-of-flight secondary ion mass spectrometry (ToF-SIMS). *Biochim. Biophys. Acta* **2011**, *1811* (11), 976-990.

(14) Sämfors, S.; Fletcher, J. S. Lipid Diversity in Cells and Tissue Using Imaging SIMS. *Annu. Rev. Anal. Chem.* **2020**, *13* (1), 249-271.

(15) Angerer, T. B.; Magnusson, Y.; Landberg, G.; Fletcher, J. S. Lipid Heterogeneity Resulting from Fatty Acid Processing in the Human Breast Cancer Microenvironment Identified by GCIB-ToF-SIMS Imaging. *Anal. Chem.* **2016**, *88* (23), 11946-11954.

(16) Eberlin, L. S.; Ferreira, C. R.; Dill, A. L.; Ifa, D. R.; Cooks, R. G. Desorption electrospray ionization mass spectrometry for lipid characterization and biological tissue imaging. *Biochim. Biophys. Acta* **2011**, *1811* (11), 946-960.

(17) Nguyen, S. N.; Kyle, J. E.; Dautel, S. E.; Sontag, R.; Luders, T.; Corley, R., . . . Laskin, J. Lipid Coverage in Nanospray Desorption Electrospray Ionization Mass Spectrometry Imaging of Mouse Lung Tissues. *Anal. Chem.* **2019**, *91* (18), 11629-11635.

(18) Bagley, M. C.; Ekelöf, M.; Muddiman, D. C. Determination of Optimal Electrospray Parameters for Lipidomics in Infrared-Matrix-Assisted Laser Desorption Electrospray Ionization Mass Spectrometry Imaging. *J. Am. Soc. Mass. Spectrom.* **2020**, *31* (2), 319-325.

(19) Caleb Bagley, M.; Garrard, K. P.; Muddiman, D. C. The development and application of matrix assisted laser desorption electrospray ionization: The teenage years. *Mass Spectrom. Rev.* **2021**, *n/a* (n/a).

(20) Ellis, S. R.; Brown, S. H.; in het Panhuis, M.; Blanksby, S. J.; Mitchell, T. W. Surface analysis of lipids by mass spectrometry: More than just imaging. *Progress in Lipid Research* **2013**, *52* (4), 329-353.

(21) Engel, K. M.; Prabutzki, P.; Leopold, J.; Nimptsch, A.; Lemmnitzer, K.; Vos, D. R. N., . . . Schiller, J. A new update of MALDI-TOF mass spectrometry in lipid research. *Progress in Lipid Research* **2022**, *86*, 101145.

(22) Römpp, A.; Spengler, B. Mass spectrometry imaging with high resolution in mass and space. *Histochem. Cell Biol.* **2013**, *139* (6), 759-783.

(23) Tran, A.; Monreal, I. A.; Moskovets, E.; Aguilar, H. C.; Jones, J. W. Rapid Detection of Viral Envelope Lipids Using Lithium Adducts and AP-MALDI High-Resolution Mass Spectrometry. *J. Am. Soc. Mass. Spectrom.* **2021**, *32* (9), 2322-2333.

(24) Jackson, S. N.; Muller, L.; Roux, A.; Oktem, B.; Moskovets, E.; Doroshenko, V. M.; Woods, A. S. AP-MALDI Mass Spectrometry Imaging of Gangliosides Using 2,6-Dihydroxyacetophenone. *J. Am. Soc. Mass. Spectrom.* **2018**, *29* (7), 1463-1472.

(25) Robinson, K. N.; Steven, R. T.; Race, A. M.; Bunch, J. The Influence of MS Imaging Parameters on UV-MALDI Desorption and Ion Yield. *J. Am. Soc. Mass. Spectrom.* **2019**, *30* (7), 1284-1293.

(26) Boskamp, M. S.; Soltwisch, J. Charge Distribution between Different Classes of Glycerophospolipids in MALDI-MS Imaging. *Anal. Chem.* **2020**, *92* (7), 5222-5230.

(27) Soltwisch, J.; Kettling, H.; Vens-Cappell, S.; Wiegelmann, M.; Müthing, J.; Dreisewerd, K. Mass spectrometry imaging with laser-induced postionization. *Science* **2015**, *348* (6231), 211-215.

(28) Ellis, S. R.; Soltwisch, J.; Paine, M. R. L.; Dreisewerd, K.; Heeren, R. M. A. Laser post-ionisation combined with a high resolving power orbitrap mass spectrometer for enhanced MALDI-MS imaging of lipids. *Chem. Commun.* **2017**, *53* (53), 7246-7249, 10.1039/C7CC02325A.

(29) Bowman, A. P.; Bogie, J. F. J.; Hendriks, J. J. A.; Haidar, M.; Belov, M.; Heeren, R. M. A.; Ellis, S. R. Evaluation of lipid coverage and high spatial resolution MALDI-imaging capabilities of oversampling combined with laser post-ionisation. *Anal. Bioanal. Chem.* **2020**, *412* (10), 2277-2289.

(30) Bookmeyer, C.; Röhling, U.; Dreisewerd, K.; Soltwisch, J. Single-Photon-Induced Post-Ionization to Boost Ion Yields in MALDI Mass Spectrometry Imaging. *Angew Chem Int Ed Engl* **2022**, e202202165.

(31) Lu, Q.; Xu, Z.; You, X.; Ma, S.; Zenobi, R. Atmospheric Pressure Mass Spectrometry Imaging Using Laser Ablation, Followed by Dielectric Barrier Discharge Ionization. *Anal. Chem.* **2021**, *93* (15), 6232-6238.

(32) Lu, Q.; Guan, X.; You, X.; Xu, Z.; Zenobi, R. High-Spatial Resolution Atmospheric Pressure Mass Spectrometry Imaging Using Fiber Probe Laser Ablation-Dielectric Barrier Discharge Ionization. *Anal. Chem.* **2021**, *93* (44), 14694-14700.

(33) Funke, S. K. I.; Bruckel, V. A.; Weber, M.; Lutzen, E.; Wolf, J. C.; Haisch, C.; Karst, U. Plug-and-play laser ablation-mass spectrometry for molecular imaging by means of dielectric barrier discharge ionization. *Anal Chim Acta* **2021**, *1177*, 338770.

(34) Elia, E. A.; Niehaus, M.; Steven, R. T.; Wolf, J.-C.; Bunch, J. Atmospheric Pressure MALDI Mass Spectrometry Imaging Using In-Line Plasma Induced Postionization. *Anal. Chem.* **2020**, *92* (23), 15285-15290.

(35) Steven, R. T.; Niehaus, M.; Taylor, A. J.; Nasif, A.; Elia, E.; Goodwin, R. J. A., . . . Bunch, J. Atmospheric-Pressure Infrared Laser-Ablation Plasma-Postionization Mass Spectrometry Imaging of Formalin-Fixed Paraffin-Embedded (FFPE) and Fresh-Frozen Tissue Sections with No Sample Preparation. *Anal. Chem.* **2022**, *94* (28), 9970-9974.

(36) Rivera, E. S.; Djambazova, K. V.; Neumann, E. K.; Caprioli, R. M.; Spraggins, J. M. Integrating ion mobility and imaging mass spectrometry for comprehensive analysis of biological tissues: A brief review and perspective. *J. Mass Spectrom.* **2020**, *55* (12), e4614.

(37) Soltwisch, J.; Heijs, B.; Koch, A.; Vens-Cappell, S.; Höhndorf, J.; Dreisewerd, K. MALDI-2 on a Trapped Ion Mobility Quadrupole Time-of-Flight Instrument for Rapid Mass Spectrometry Imaging and Ion Mobility Separation of Complex Lipid Profiles. *Anal. Chem.* **2020**, *92* (13), 8697-8703.

(38) Meier, F.; Brunner, A. D.; Koch, S.; Koch, H.; Lubeck, M.; Krause, M., . . . Mann, M. Online Parallel Accumulation-Serial Fragmentation (PASEF) with a Novel Trapped Ion Mobility Mass Spectrometer. *Mol. Cell. Proteomics* **2018**, *17* (12), 2534-2545.

(39) Pauling, J. K.; Hermansson, M.; Hartler, J.; Christiansen, K.; Gallego, S. F.; Peng, B., . . . Ejsing, C. S. Proposal for a common nomenclature for fragment ions in mass spectra of lipids. *PLoS One* **2017**, *12* (11), e0188394.

(40) Liebisch, G.; Fahy, E.; Aoki, J.; Dennis, E. A.; Durand, T.; Ejsing, C. S., . . . Spener, F. Update on LIPID MAPS classification, nomenclature, and shorthand notation for MS-derived lipid structures. *J. Lipid Res.* **2020**, *61* (12), 1539-1555.

(41) Pham, H. T.; Maccarone, A. T.; Thomas, M. C.; Campbell, J. L.; Mitchell, T. W.; Blanksby, S. J. Structural characterization of glycerophospholipids by combinations of ozone- and collision-induced dissociation mass spectrometry: the next step towards "top-down" lipidomics. *Analyst* **2014**, *139* (1), 204-214, 10.1039/C3AN01712E.

(42) Williams, P. E.; Klein, D. R.; Greer, S. M.; Brodbelt, J. S. Pinpointing Double Bond and sn-Positions in Glycerophospholipids via Hybrid 193 nm Ultraviolet Photodissociation (UVPD) Mass Spectrometry. *J. Am. Chem. Soc.* **2017**, *139* (44), 15681-15690.

(43) Niehaus, M.; Robinson, K. N.; Murta, T.; Elia, E. A.; Race, A. M.; Yan, B., . . . Bunch, J. MALDI-2 at Atmospheric Pressure—Parameter Optimization and First Imaging Experiments. *J. Am. Soc. Mass. Spectrom.* **2020**, *31* (11), 2287-2295.

(44) Fouquet, T.; Barrère-Mangote, C.; Farenc, M.; Afonso, C.; Giusti, P. Atmospheric solid analysis probe mass spectrometry vs electrospray tandem mass spectrometry of polydimethylsiloxanes in positive and negative ionization modes. *Rapid Commun. Mass Spectrom.* **2015**, *29* (10), 982-986.

(45) Schlosser, A.; Volkmer-Engert, R. Volatile polydimethylcyclosiloxanes in the ambient laboratory air identified as source of extreme background signals in nanoelectrospray mass spectrometry. *J. Mass Spectrom.* **2003**, *38* (5), 523-525.

(46) Gyr, L.; Klute, F. D.; Franzke, J.; Zenobi, R. Characterization of a Nitrogen-Based Dielectric Barrier Discharge Ionization Source for Mass Spectrometry Reveals Factors Important for Soft Ionization. *Anal. Chem.* **2019**, *91* (10), 6865-6871.

(47) Murphy, R. C.; Axelsen, P. H. Mass spectrometric analysis of long-chain lipids. *Mass Spectrom. Rev.* **2011**, *30* (4), 579-599.

(48) Wan, C.; Wu, W.; Liu, S.; Song, H.; Yang, Y.; Zheng, C.; Gao, X. Effect of Gas Components and Particulate Matter on the Conversion of Nitric Oxide by Dielectric Barrier Discharge. *Energy & Fuels* **2021**, *35* (8), 6711-6724.

(49) Palmer, A.; Phapale, P.; Chernyavsky, I.; Lavigne, R.; Fay, D.; Tarasov, A., . . . Alexandrov, T. FDR-controlled metabolite annotation for high-resolution imaging mass spectrometry. *Nat. Methods* **2017**, *14* (1), 57-60.